

## Anisotropy of the spin-polarized edge current in monolayer transition metal dichalcogenide zigzag nanoribbons

J. H. Correa,<sup>1,2</sup> A. C. Dias,<sup>2</sup> L. Villegas-Lelovsky,<sup>3,4</sup> Jiyong Fu,<sup>1,\*</sup> Leonor Chico,<sup>5</sup> and Fanyao Qu<sup>2,†</sup>

<sup>1</sup>*Department of Physics, Qufu Normal University, 273165, Qufu, Shandong, China*

<sup>2</sup>*Instituto de Física, Universidade de Brasília, Brasília-DF 70919-970, Brazil*

<sup>3</sup>*Departamento de Física, IGCE, Universidade Estadual Paulista, 13506-900 Rio Claro, São Paulo, Brazil*

<sup>4</sup>*Departamento de Física, Centro de Ciências Exatas e de Tecnologia, Universidade Federal de São Carlos, São Carlos, São Paulo 13565-905, Brazil*

<sup>5</sup>*Instituto de Ciencia de Materiales de Madrid, Consejo Superior de Investigaciones Científicas, C/ Sor Juana Inés de la Cruz 3, 28049 Madrid, Spain*



(Received 22 November 2019; accepted 15 April 2020; published 15 May 2020)

We report anisotropic spin polarization of edge currents in MoS<sub>2</sub> and WS<sub>2</sub> monolayer zigzag nanoribbons (ZNRs) deposited on either nonmagnetic or ferromagnetic insulator substrates. We employ an 11-band tight-binding model to calculate the electronic band structures of transition metal dichalcogenide (TMDC) monolayers and their corresponding nanoribbons in the presence of Rashba spin-orbit coupling (RSOC) and magnetic proximity effect produced by ferromagnetic substrate. We adopt the nonequilibrium Green's function method together with Landauer-Büttiker formalism to study the quantum transport behavior stemming from the edge states of ZNRs. We demonstrate that the spin-polarized edge current can be generated in both MoS<sub>2</sub> and WS<sub>2</sub> ZNRs with RSOC. We find that the spin polarization spreads out in all three directions. This is in stark contrast to what occurs in zigzag graphene nanoribbons, for which the polarization only exists in the transverse direction (across the width of ribbons). In addition, the spin polarization direction strongly depends on the strength of the intrinsic SOC component. The interplay of Rashba and intrinsic SOC is crucial for the spin polarization of the currents in any spatial direction. For TMDCs with stronger intrinsic SOC such as in WS<sub>2</sub> monolayer ZNRs, we observe that the spin polarization along the perpendicular direction to the plane of the ZNR can be as large as 90%. Moreover, the unusual anisotropy of the spin polarization can be further enhanced by the magnetic proximity effect. These results open up possibilities for the generation of tunable high-spin polarization currents in ZNRs without application of an external magnetic field.

DOI: [10.1103/PhysRevB.101.195422](https://doi.org/10.1103/PhysRevB.101.195422)

### I. INTRODUCTION

Since the landmark achievement of graphene [1], two-dimensional (2D) materials such as transition metal dichalcogenides (TMDCs) have been extensively explored due to their unique chemical and physical properties, as well as their great potential for postsilicon electronics [2,3]. Unlike graphene, the inversion asymmetry together with strong spin-orbit coupling (SOC) in the monolayer TMDCs (MoS<sub>2</sub>, MoSe<sub>2</sub>, WS<sub>2</sub>, WSe<sub>2</sub>) leads to spin splitting and spin-valley locking, giving rise to intriguing characteristics for spintronics and valleytronics. In addition, tungsten (W)-based compounds exhibit a spin-orbit splitting approximately twice as large as that of molybdenum (Mo)-based ones, and the signs of the conduction band spin-orbit splittings in W- and Mo-based TMDCs are opposite. Therefore, their optical properties are quite different, e.g., Mo compounds are bright materials and W-based ones are darkish for the ground states [2,4–7].

This large spin splitting, especially in the valence band, in turn, suppresses the spin relaxation and results in long spin

lifetimes. Moreover, due to the large valley separation in the momentum space, the decay of valley polarization through the intervalley scattering mediated by low-energy phonons is typically slow. Therefore, carriers in TMDCs usually possess long valley lifetimes [8]. These features are greatly important for spintronic and valleytronic applications, in which the charge, spin, and valley degrees of freedom are exploited. Hence, relevant proposals based on TMDCs have gained significant impact on the current technology-oriented research [9,10]. Recently, TMDC nanoribbons have been successfully synthesized by several methods [11–13], ranging from chemical to mechanical routes, mostly zigzag-terminated. Although great progress has been made experimentally, the theoretical understanding of the properties of these systems still remains very elusive. This brings forth the question of their spin-dependent transport properties in comparison to those of GNRs, which are more widely explored.

As known, intrinsic SOC in graphene is negligible, but the occurrence of spin-dependent transport in graphene nanoribbons (GNRs) with extrinsic Rashba SOC (RSOCs), which are generated by an external applied electric field has been previously predicted [14], both in armchair-terminated and zigzag ones. Furthermore, the spin polarization is mainly along the transversal direction of GNRs, while the

\*yongjf@qfnu.edu.cn

†fanyao@unb.br

perpendicular and longitudinal components are vanishingly small [14,15]. There are different routes to modify these features: for example, vacancies that break the longitudinal mirror symmetry of the ribbons, such as square notches, allow for nonzero spin polarization in all directions [16]. Also, in bilayer GNRs, the transversal spin polarization can be further enhanced by the interplay of RSOC and an asymmetric double-gate voltage [17]. Finally, corrugated ZGNRs, i.e., nanoribbons that contain multiple RSOC regions, may deliver significantly enhanced spin polarizations [18].

Besides SOC, the edges of zigzag graphene and TMDC ribbons are also fundamentally different. Specifically, the atoms at both edges of ZGNRs are obviously the same, all carbon [14], whereas in TMDC ribbons they correspond to different atomic species and hence the corresponding longitudinal symmetry is always broken. Independent of the number of zigzag chains across the ribbon width, the edge termination is similar (while Mo atoms are located at one edge, S atoms are at the other edge), and edge states have a similar behavior. However, when the ribbon width changes, the transport properties of TMDC ZNRs changes at higher energy ranges. Since the transport properties of a system are closely correlated to its electronic band structure, one can infer that the transport properties of ZGNRs are quite different than those of TMDC zigzag nanoribbons (ZNRs). Analogously, quantum transport in Mo-based TMDC ribbons should also differ from that of its W-based counterparts because of their distinct spin-orbit ordering in the band structure.

Therefore, a comparative study of the transport properties of TMDC and graphene ZNRs is crucial for understanding the roles of intrinsic SOC and extrinsic RSOC in different materials with different spin-orbit strength as well as of the structure of ribbon edges in the carrier transport. Moreover, considering the magnetic proximity effect in TMDCs induced by ferromagnetic (FM) insulator substrates [19–24], which lifts the valley degeneracy, it is also essential to demonstrate how the exchange field and its combined effect with spin-orbit field affect spin-dependent transport. This, together with underlying physics of the spin-polarization anisotropy, remains elusive and yet to be understood.

In this paper, we develop a comprehensive theory about anisotropic spin polarization of edge current in monolayer MoS<sub>2</sub> and WS<sub>2</sub> ZNRs deposited on either nonmagnetic or ferromagnetic insulator substrates, involving intrinsic SOC and external RSOC as well as magnetic proximity effects on quantum transport. These hybrid systems could be used as robust tunable spin (valley) filters for diverse applications. We focus our attention on the anisotropy of spin polarization in carrier transport. We observe that spin-polarized edge current can be generated in both MoS<sub>2</sub> and WS<sub>2</sub> ZNRs with RSOC. Unlike ZGNRs in which spin polarization is only along the transverse direction, here the spin polarization spreads out in all three directions and shows a strong anisotropy. We explain this effect as a competition between intrinsic and RSOC. Moreover, the largest spin polarization component is no longer along the transversal (*y*) direction of TMDC ZNRs as in GNRs. Interestingly, the spin polarization along the *z* direction can reach 90% of its total value in TMDCs with stronger intrinsic SOC, such as WS<sub>2</sub> monolayer ZNRs.

Furthermore, this unusual anisotropy can be further enhanced by the magnetic proximity effect.

This paper is organized as follows: In Sec. II, we present our 11-band tight-binding (TB) model and theoretical framework for the calculation of the quantum transport properties such as spin quantum conductance and spin polarization. In Sec. III, we discuss our results. Finally, we present the conclusions in Sec. IV.

## II. THEORETICAL MODEL

In this section, we first introduce the Hamiltonian, including intrinsic SOC, extrinsic RSOC, and exchange field interaction within the TB approximation. Then, we present the theoretical framework of nonequilibrium Green's functions and Landauer-Büttiker formalism, used to determine quantum transport properties, including quantum conductance and spin polarization of current through TMDC ZNRs.

### A. Multiband tight-binding model for TMDC monolayers

A TMDC monolayer is composed of one layer of transition-metal atoms *M* sandwiched between top and bottom layers of chalcogen atoms *X*. Considering five *d* orbitals from the *M* atom and six *p* orbitals of *X* atoms in the top and bottom layers, i.e.,  $p_x^t, p_y^t, p_z^t, d_{3z^2-r^2}, d_{x^2-y^2}, d_{xy}, d_{yz}, d_{zx}, p_x^b, p_y^b, p_z^b$ , we construct an 11-band model for the TMDC monolayer. The second-nearest-neighbor hopping terms for both *M* and *X* atoms are taken into account. The total Hamiltonian for the TMDC monolayers grown on ferromagnetic insulator substrate reads

$$H = H_0 + H_R + H_{ex}, \quad (1)$$

where the first term is the Hamiltonian of pristine TMDC monolayers, the second one denotes the RSOC Hamiltonian, and the third term corresponds to the exchange interaction produced by a ferromagnetic substrate. By applying a unitary transformation, we decouple the total Hamiltonian into different subspaces with even and odd symmetries. More details about the decoupling in even and odd subspaces can be found in Ref. [25].

### 1. Multiband tight-binding model for pristine TMDC monolayers

In second quantization language,  $H_0$  is written as

$$\begin{aligned} H_0 = & \sum_{i,\mu,s} (E_{i,\mu,s}^M a_{i,\mu,s}^\dagger a_{i,\mu,s} + E_{i,\mu,s}^X b_{i,\mu,s}^\dagger b_{i,\mu,s}) \\ & + \sum_{\langle i,j \rangle, \mu, \nu, s} t_{i,j;\mu,\nu}^{MX} a_{i,\mu,s}^\dagger b_{j,\nu,s} \\ & + \sum_{\langle\langle i,j \rangle\rangle, \mu, \nu, s} (t_{i,j;\mu,\nu}^{MM} a_{i,\mu,s}^\dagger a_{j,\nu,s} + t_{i,j;\mu,\nu}^{XX} b_{i,\mu,s}^\dagger b_{j,\nu,s}) \\ & + \sum_{\langle\langle\langle i,j \rangle\rangle\rangle, \mu, \nu, s} (t_{i,j;\mu,\nu}^{MM} a_{i,\mu,s}^\dagger a_{j,\nu,s} + t_{i,j;\mu,\nu}^{XX} b_{i,\mu,s}^\dagger b_{j,\nu,s}) \\ & + \sum_{i,\mu,s,\nu,s'} \lambda_{\mu,\nu,s,s'} (a_{i,\mu,s}^\dagger a_{i,\nu,s'} + b_{i,\mu,s}^\dagger b_{i,\nu,s'}) + \text{H.c.} \quad (2) \end{aligned}$$

Here  $i$  and  $j$  run over the lattice sites,  $\nu$  and  $\mu$  denote the orbitals,  $a_{i,\mu,s}$  ( $a_{i,\mu,s}^\dagger$ ) is the annihilation (creation) operator of an electron in transition metal sites ( $M = \text{Mo}, \text{W}$ ), and  $b_{i\mu s}$  ( $b_{i\mu s}^\dagger$ ) refers to the corresponding annihilation (creation) operator at chalcogen sites ( $X = \text{S}, \text{Se}, \text{Te}$ ).  $\langle \rangle$ ,  $\langle \langle \rangle \rangle$ , and  $\langle \langle \langle \rangle \rangle \rangle$  indicate the sum over all the nearest, next-nearest, and next-next-nearest neighbor sites, respectively. In Eq. (2), the first and second terms comprise the on-site energies for both elements of  $M$  and  $X$  atoms, respectively, the third term contains the first nearest-neighbor hoppings, and the fourth and fifth terms describe hoppings within the same elements.  $\lambda_{\mu,s,\nu,s'}$  is the intrinsic SOC parameter, with  $s, s'$  indicating the spin orientation. Here, we consider  $\text{MoS}_2$  and  $\text{WS}_2$  as our starting materials. The corresponding intrinsic SOC parameters are  $\lambda_{Mo} = -0.0806$  eV,  $\lambda_W = 0.2754$  eV, and  $\lambda_S = -0.052$  eV, and H.c. stands for Hermitian conjugate. For more details about our TB calculation implementation under the second-nearest-neighbor hopping approximation of both transition metals and chalcogenide atoms, as well as relevant intrinsic spin-orbit parameters for other TMDCs monolayers, see Ref. [25].

## 2. Multiband tight-binding model for Rashba spin-orbit coupling

With the Hamiltonian of the pristine TMDC monolayers at hand, we can straightforwardly extend our study to the TMDCs with RSOC, which can be generated by breaking the structural inversion symmetry due to a substrate. The RSOC intensity can be tuned by the application of an external electric field [14,26,27]. The effective Rashba interaction in the second-quantization picture reads

$$H_R = i\lambda_R \sum_{(i,j),\mu,s,s'} \frac{1}{|\vec{r}_{i,j}|} (\vec{\sigma}_{s,s'} \times \vec{r}_{i,j})_z c_{i,\mu,s}^\dagger c_{j,\mu,s'} + \text{H.c.}, \quad (3)$$

where  $c_{i,\mu,s}^\dagger$  ( $c_{i,\mu,s}$ ) =  $a_{i,\mu,s}^\dagger$  ( $a_{i,\mu,s}$ ),  $b_{i,\mu,s}^\dagger$  ( $b_{i,\mu,s}$ ) ( $a_{i,\mu,s}$ ,  $b_{i,\mu,s}$ ),  $\lambda_R$  is the RSOC parameter,  $\vec{\sigma}$  are the Pauli matrices, and  $\vec{r}_{i,j}$  is the distance vector between nearest neighbors at  $i$  and  $j$  sites.

## 3. Multiband tight-binding model for the exchange field interaction

We assume that the exchange field is produced by a ferromagnetic substrate perpendicular to the plane of the monolayer. It breaks time-reversal symmetry, leading to the removal of spin degeneracy. The Hamiltonian for the exchange interaction is

$$H_{\text{ex}} = \lambda_{\text{ex}} \sum_{i,\mu,s,s'} [\hat{m} \cdot \vec{\sigma}_{s,s'}] c_{i,\mu,s}^\dagger c_{i,\mu,s'} + \text{H.c.}, \quad (4)$$

with  $\lambda_{\text{ex}}$  being the exchange field parameter and  $\hat{m}$  the unit vector along the magnetization direction.

## B. Multiband tight-binding model for TMDC zigzag nanoribbons

Pristine TMDC ZNRs, as shown in Fig. 1, maintain the periodicity along the transport direction ( $x$  axis), while the carriers are confined due to the edges across their widths, that we take as the  $y$  direction. To take into account all the

hoppings in Eq. (2), we have doubled the size of the unit cell with respect to that usually employed in the literature [see dashed rectangular box in Fig. 1(b)]. Regarding the interaction between one unit cell and the adjacent ones, we denote  $H_{n,n+1}$  and  $H_{n,n-1}$ , respectively. Taking advantage of the translational symmetry in the transport direction, we then write down the Hamiltonian which depends on the wave vector ( $k_x$ ),

$$H = H_{n,n+1} e^{2ik_x a} + H_{n,n} + H_{n,n-1} e^{-2ik_x a}, \quad (5)$$

where  $H_{n,n}$  denotes the Hamiltonian containing the interactions in the  $n$ th unit cell and  $a$  is the lattice constant, which is 0.316 nm for  $\text{MoS}_2$  and 0.315 nm for  $\text{WS}_2$ . In this section, it is sufficient to consider only the even subspace, since it describes very well the transport properties at the Fermi level [25]. The matrix elements of RSOC and exchange field interaction for TMDC ZNRs are calculated in Appendixes A and B, respectively.

## C. Quantum transport

A powerful tool to study transport properties is the nonequilibrium surface Green's function (NEGF) method [28]. The foremost advantages of this framework are its simplicity and low computational cost. Our system comprises three parts, as shown in Fig. 1(b): the central or scattering region indicated by C and the left ( $L$ ) and right ( $R$ ) semi-infinite leads. The length of the central transport region is determined by  $l$  and the width of the system by  $W$ , given by the number of zigzag lines ( $N$ ). The influence of the leads on the central part is considered via a self-energy ( $\Sigma_{L,R}$ ) correction. The electrical conductance per spin channel is calculated in real space by means of the Landauer-Büttiker formalism [29,30],

$$G_{ss'} = G_o \text{Tr} \{ \Gamma_s^L(\epsilon) \mathcal{G}_{C,ss'}^r(\epsilon) \Gamma_{s'}^R(\epsilon) \mathcal{G}_{C,s's}^a(\epsilon) \}, \quad (6)$$

where  $G_o = e^2/h$  is the quantum conductance unit.  $\text{Tr}\{\dots\}$  refers to the trace of the product of the retarded [ $\mathcal{G}_{C,ss'}^r(\epsilon)$ ] and advanced [ $\mathcal{G}_{C,s's}^a(\epsilon)$ ] Green's functions of the central part as well as their couplings to the leads  $\Gamma_s^j(\epsilon)$  ( $j = L, R$ ), with  $E$  the energy and  $\eta \rightarrow 0^+$  is a real infinitesimal quantity. To calculate  $\mathcal{G}_C^r(z)$  and  $\mathcal{G}_C^a(z)$ , we employ  $\epsilon = E - i\eta$  and  $\epsilon = E + i\eta$ , respectively. The Green's function of the two-terminal device per spin is given by

$$\mathcal{G}_{C,ss'}^{r,a}(\epsilon) = [\epsilon - H_{C,ss'} - \Sigma_s^L(\epsilon) - \Sigma_s^R(\epsilon)]^{-1}, \quad (7)$$

where  $H_{C,ss'}$  is the Hamiltonian of the central part per spin,  $\Sigma_s^j(\epsilon) = H_{j,C}^\dagger g_j^j(z) H_{j,C}$  ( $j = L, R$ ) are the spin-diagonal self-energies,  $H_{j,C}$  is the Hamiltonian matrix describing the coupling between the central part and the leads, and  $g_j$  are the Green's function of the semi-infinite leads, which are calculated iteratively [30,31] (see Appendix C). We define the couplings to the leads  $\Gamma_s^{L,R}$  as

$$\Gamma_s^j(\epsilon) = i \{ \Sigma_s^j(\epsilon) - [\Sigma_s^j(\epsilon)]^\dagger \} \quad (j = L, R). \quad (8)$$

With Eq. (6), the total conductance can be calculated as follows:

$$G = \sum_{ss'} G_{ss'} = G_{\uparrow\uparrow} + G_{\uparrow\downarrow} + G_{\downarrow\uparrow} + G_{\downarrow\downarrow}. \quad (9)$$

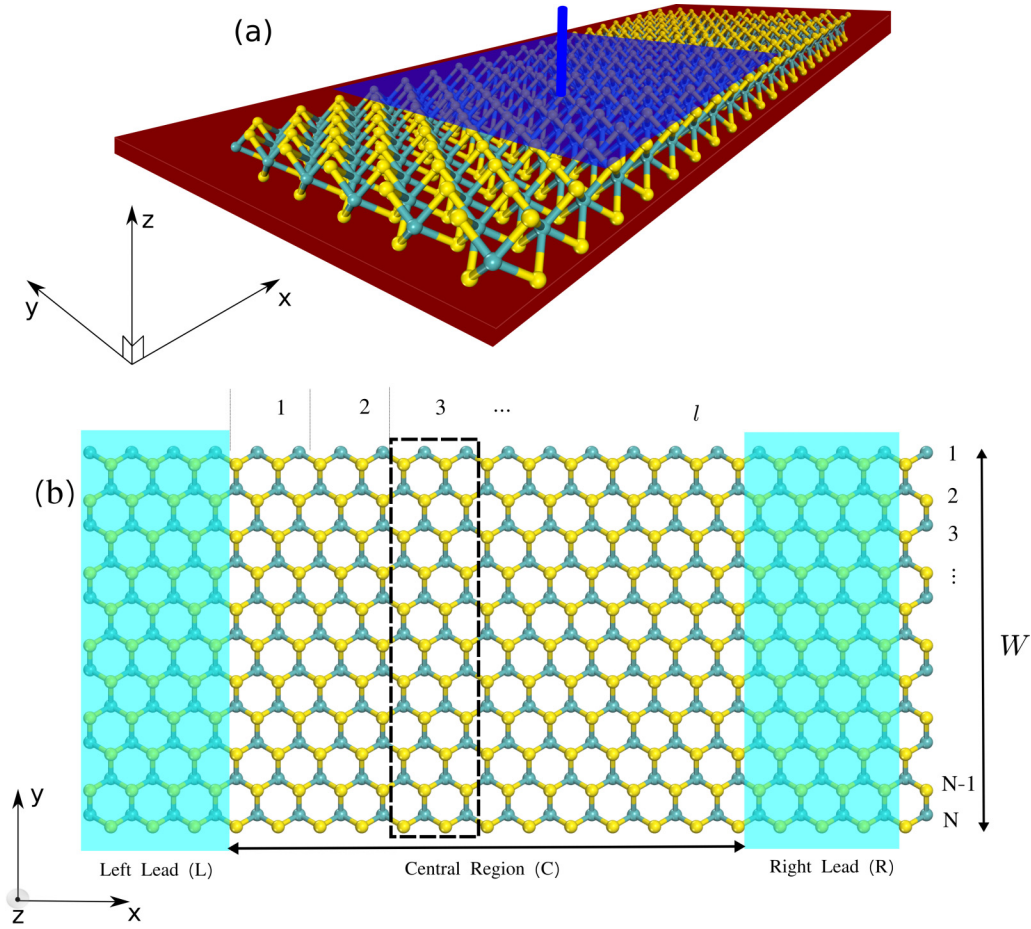


FIG. 1. (a) Perspective view of zigzag TMDC nanoribbon device containing a front-back gate voltage (blue slab). (b) Top view of the zigzag TMDC nanoribbon device, composed of a central region (C) connected to the left (L) and right (R) semi-infinite leads (marked in cyan), where  $l$  is the number of unit cells (rectangular box) of the central part and  $W$  is its width, given by the number of zigzag lines ( $N$ ).

With the Green's function of the conductor at hand, the total density of states (DOS) can be obtained by

$$\text{DOS}(E) = -\frac{1}{\pi} \text{Im} \text{Tr} \left[ \sum_{ss'} \mathcal{G}_{C,ss'}^r(\epsilon) \right]. \quad (10)$$

Another crucial physical quantity which is used to characterize the current is the spin polarization, defined by [32]

$$P_\alpha = \frac{I_{j,\alpha}^\uparrow - I_{j,\alpha}^\downarrow}{I_{j,\alpha}^\uparrow + I_{j,\alpha}^\downarrow}, \quad (11)$$

where  $I_{j,\alpha}^\uparrow$  and  $I_{j,\alpha}^\downarrow$  represent the currents flowing through lead  $j$  chosen along the  $\alpha$  direction with spin-up and spin-down components, respectively. In terms of the Green's function, this equation can be written as [16,17,27]

$$P_\alpha = \frac{G_0 \text{Tr} [\sigma_\alpha \Gamma_s^L(\epsilon) \mathcal{G}_{C,ss'}^r(\epsilon) \Gamma_{s'}^R(\epsilon) \mathcal{G}_{C,s's}^a(\epsilon)]}{G}, \quad (12)$$

where  $\sigma_\alpha$  are the corresponding Pauli matrices with  $\alpha = x, y, z$ . The projections of spin polarization along the  $x$ ,  $y$ , and  $z$  directions, i.e.,  $P_x$ ,  $P_y$ , and  $P_z$  are the parallel, transversal, and perpendicular ones, respectively. Clearly, the total

polarization labeled by  $P_t$  can be quantified as

$$P_t = \sqrt{P_x^2 + P_y^2 + P_z^2}. \quad (13)$$

It is clear from the previous definition that the total polarization must obey current conservation, with  $P_t \leq 1$ .

### III. RESULTS AND DISCUSSIONS

In this section, we first present the electronic band structures of pristine MoS<sub>2</sub> and WS<sub>2</sub> monolayers, and then we discuss the effects of RSOC, exchange field, and the combination of both. This serves as a reference for the electronic band structures of nanoribbons in the presence of RSOC, exchange field, and both effects, that we present afterward. Finally, we discuss the transport properties, focusing on the anisotropy of the spin polarization. It is worthwhile to recall that although we focus mainly on the narrow TMDC ZNRs, the behavior of the edge current is also applicable to wider nanoribbons due to the central role of edge states for this edge termination [33].

#### A. Band structure of pristine TMDCs monolayers

To gain better insight of quantum transport property, let us start with the simplest case, corresponding to the electronic

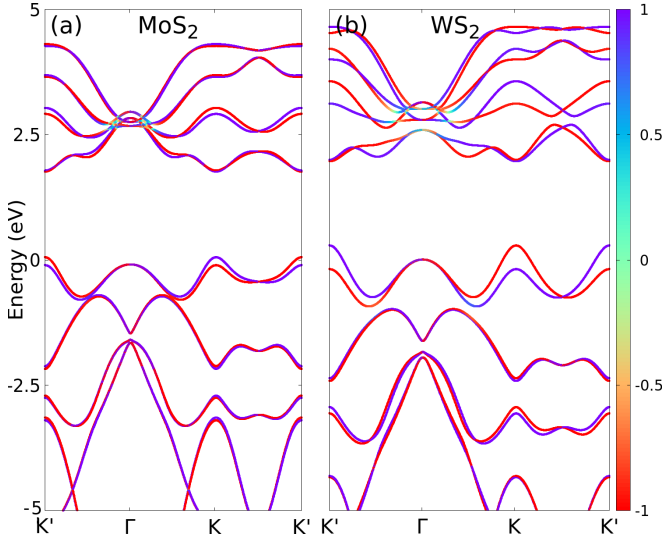


FIG. 2. Electronic band structure of monolayer MoS<sub>2</sub> (a) and WS<sub>2</sub> (b) including intrinsic SOC only. Colors indicate the  $z$  component of the spin ( $\langle S_z \rangle$ ).

band structure in pristine TMDCs monolayers, considering only intrinsic SOC, i.e., without extrinsic RSOC and exchange field, as shown in Figs. 2(a) and 2(b) for the monolayer MoS<sub>2</sub> and WS<sub>2</sub>, respectively (for that, we made a Fourier transformation of Eq. (2) in order to work in the reciprocal space). The intrinsic SOC gives rise to spin splitting at the high symmetry  $K$  and  $K'$  points of both the conduction and valence bands. The lack of spatial inversion symmetry combined with strong intrinsic SOC leads to the so-called spin-valley locking, i.e., the spin splittings in the two inequivalent  $K$  and  $K'$  valleys have the same magnitude but opposite signs. The spin splitting of the valence band, arising primarily from the transition-metal  $d$  orbitals, is around hundreds of meV, which is far greater than that of the conduction band, ranging from several to tens of meV. From our 11-band TB calculations, which account for the second-nearest-neighbor hopping terms of both transition-metal and chalcogenide atoms, we obtain a conduction (valence) band splitting of 21 meV (158 meV) in monolayer MoS<sub>2</sub>, and 27 meV (472 meV) in monolayer WS<sub>2</sub>. These values are in good agreement with recent reports in the literature [34]. Note that the spin-splitting energy grows with the increase of the intrinsic SOC parameter, which depends on the atomic species. Consequently, the spin splitting is more significant in W-based TMDCs than that in Mo-based ones, cf. the  $K$  ( $K'$ ) splittings in Figs. 2(a) and 2(b). Furthermore, from Figs. 2(a) and 2(b), we can also see that the order of spin-up and spin-down states for the topmost valence band in the  $K$  ( $K'$ ) valley in WS<sub>2</sub> is reverted, as compared to that in MoS<sub>2</sub>. In contrast to the  $K$  ( $K'$ ) point, the electronic band structure in the  $\Gamma$  point remains spin degenerate, as a result of the Kramer degeneracy.

### B. Effects of RSOC and exchange field on the band structure of TMDC monolayers

Let us consider now the effect of extrinsic RSOC and exchange field on the electronic band structure. To analyze this systematically, we first focus on the Rashba effect (i.e.,

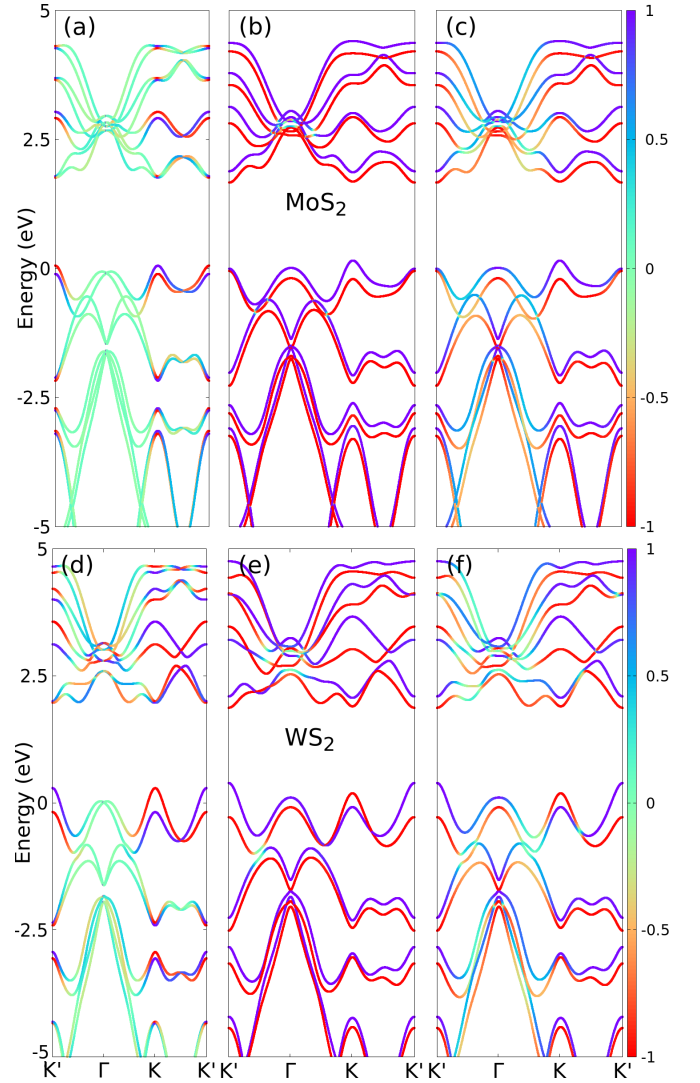


FIG. 3. Electronic band structure of monolayer MoS<sub>2</sub> [(a)–(c)] and WS<sub>2</sub> [(d)–(f)]. The left [(a), (d)], middle [(b), (e)], and right [(c), (f)] panels are for the cases of RSOC, exchange field, and both of them, respectively. The colors represent the  $z$  component of the spin ( $\langle S_z \rangle$ ). The strength of RSOC  $\lambda_R = 0.05$  eV and exchange field  $\lambda_{ex} = 0.1$  eV are considered. The direction and magnitude are indicated by the sign and number in the color bar.

without exchange field), then we study the effect of exchange field only, and further discuss their combined effects.

In Figs. 3(a) and 3(d), we show the band structure of monolayer MoS<sub>2</sub> and WS<sub>2</sub>, respectively, calculated using Eq. (2) and solely the extrinsic RSOC given by Eq. (3). Similar to the usual Rashba scenario in conventional semiconductor nanostructures, we observe a band shift of the two spin branches with respect to the  $\Gamma$  point ( $\mathbf{k} = 0$ ) of the band structure. In other words, a crossing (commonly called saddle point) between two spin branches at  $\mathbf{k} = 0$  is formed, while for finite  $\mathbf{k}$  the spin degeneracy is lifted because of the structural inversion symmetry breaking, which induces a nonzero RSOC. The strength of the Rashba spin-splitting energy depends on the Rashba coefficient, which can be controlled by the intensity of external electric field or the type of substrate. This remarkable band splitting was also previously mentioned in Ref. [26],

where the authors present first principles calculations, showing that it is feasible to achieve the same effect by preparing a MoS<sub>2</sub> monolayer on a bilayer Bi(111) substrate. It is worth noting that the spin-up and spin-down states around the  $\Gamma$  point are fully mixed, and hence the spin is no longer a good quantum number. This can be clearly seen from the color of the bands in the vicinity of the  $\Gamma$  point, which indicates the  $z$  component of spin  $\langle S_z \rangle \sim 0$ , whereas the RSOC is less pronounced around the  $K$  and  $K'$  points.

Figures 3(b) and 3(e) display the band structures of monolayer MoS<sub>2</sub> and WS<sub>2</sub>, respectively, deposited on a FM substrate [19]. We assume that the FM substrate produces an out-of-plane exchange field. Note that the intrinsic SOC together with broken inversion symmetry leads to a spin-valley locked band structure. Time-reversal symmetry requires the SOC splitting to produce identical values for the  $K$  and  $K'$  valleys. However, a FM exchange interaction breaks time-reversal symmetry and lifts the spin degeneracy even at the  $\Gamma$  point. It always lowers the energy of spin-down bands and raises the energy of the spin-up bands. Hence, the exchange field competes with the spin-orbit splitting in the  $K$  valley, while it enlarges the spin-orbit conduction band gap in the  $K'$  valley, leading to a valley-contrasting behavior, see Figs. 3(b) and 3(e) in which the lowest conduction bands around  $K$  and  $K'$  have the same spin states. In addition, since the exchange field does not have an in-plane component, there is no spin mixing in the band structure. Therefore, the spin remains a good quantum number, as shown in the colors of the band structure near the  $\Gamma$ ,  $K$ , and  $K'$  points, where the spin-up and spin-down states can be easily distinguished. All these features are in stark contrast to those found considering only the RSOC, cf. Figs. 3(a) and 3(d), with very small spin components around  $\Gamma$ .

In Figs. 3(c) and 3(f), we show the combined effect of both RSOC and exchange field on the band structure. It is clear from the figures that a considerable spin splitting occurs around the  $\Gamma$  point. Likewise, due to the exchange field, there are more bands with spin-up and spin-down in the  $z$  direction than for the Rashba-only cases.

### C. Edge states of pristine TMDC zigzag nanoribbons

Now we are ready to focus our attention on the edge states of pristine TMDC ZNRs, obtained by solving Eq. (5) in the absence of both extrinsic RSOC and exchange field. In Fig. 4(a) [Fig. 4(d)], we show the band structure of MoS<sub>2</sub> (WS<sub>2</sub>) ZNRs, including only intrinsic SOC. The width ( $W$ ) of the ribbon is fixed at  $N = 10$ . The edge states emerge in both MoS<sub>2</sub> and WS<sub>2</sub> nanoribbons. Before discussing the electronic band structure in detail (as shown below in Fig. 4), we first take a look at the DOS, especially in the energy range corresponding to the edge states, see Figs. 4(b) and 4(e) for MoS<sub>2</sub> and WS<sub>2</sub> nanoribbons, respectively. The van Hove singularities are seen as sharp peaks at each energy subband; basically this is due to the 1D character of these systems. Because of the peaked DOS which comes from the edge states, metallic behavior and the corresponding conduction channels are expected. We show the total spin conductance for MoS<sub>2</sub> and WS<sub>2</sub> nanoribbons in Figs. 4(c) and 4(f), respectively. We can see that the conductance increases in steps of

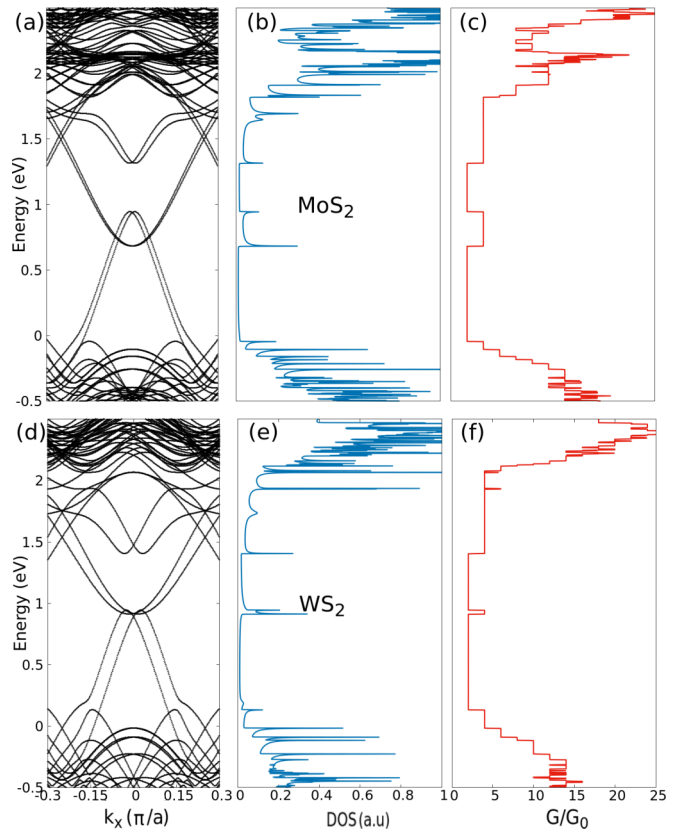


FIG. 4. (a) Electronic band structure, (b) density of states, and (c) total quantum conductance for MoS<sub>2</sub> ZNR. (d)–(f) The corresponding results for WS<sub>2</sub> ZNR. The width of ZNRs is chosen as  $N = 10$ .

$2G_0$ : More conducting channels open with increasing energy. The conductance shows plateaus and they increase with the number of subbands occurring below the Fermi energy [35].

### D. Effects of RSOC and exchange field on the edge states of TMDC zigzag nanoribbons

Here we focus on the band structure of TMDC ZNRs. To better appreciate the effect of external RSOC and exchange field, we first analyze the ribbons in the presence of intrinsic SOC only. Figure 5 zooms the bands around the energies of the edge states for MoS<sub>2</sub> (a) and for WS<sub>2</sub> ZNRs (b). Remarkably, it is found that the branches of spin-up and spin-down edge states are shifted with respect to the point at  $k_x = 0$ , even without the inclusion of external RSOC. In other words, the intrinsic SOC alone shifts the spin-up branch to one direction in  $k$  space and the spin-down branch in the opposite direction, leading to the crossing of the bands with opposite spin at  $k_x = 0$  [36]. This is in contrast to the bulk 2D monolayers, for which the bands are spin degenerate near the  $\Gamma$  point, cf. Figs. 2(a) and 2(b).

It is important to remark that the shift of edge spin bands in nanoribbons without external RSOC is similar to that occurring in bulk 2D monolayers with RSOC. However, the spin properties are fundamentally distinct. In the bulk 2D case, there is a considerable spin mixing around the  $\Gamma$  point, while for ZNRs the spin remains a good quantum number.

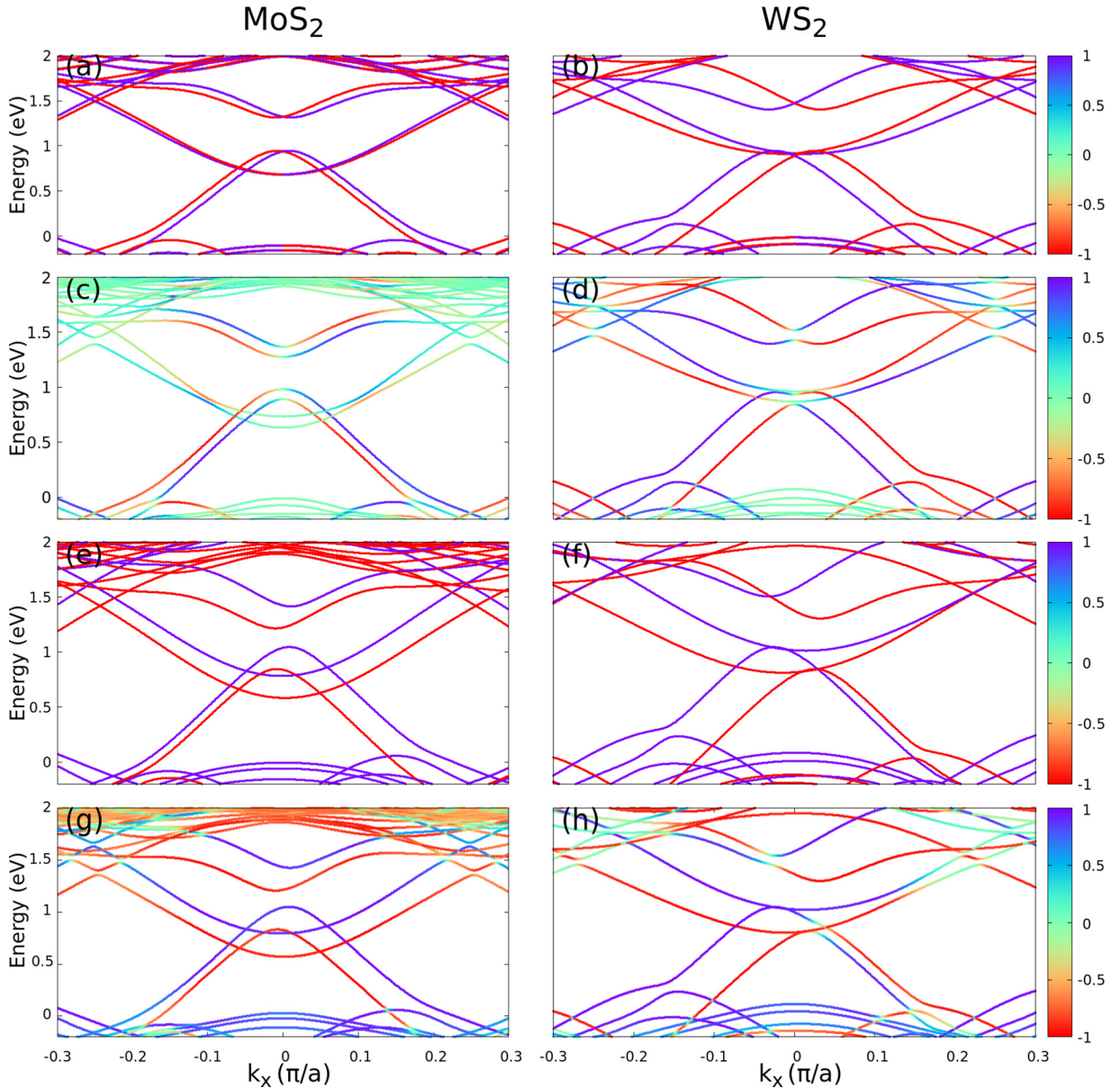


FIG. 5. Electronic band structure of MoS<sub>2</sub> (left panels) and WS<sub>2</sub> (right panels) ZNRs, for  $(\lambda_R, \lambda_{ex}) = (0, 0)$  [(a), (b)],  $(0.05, 0)$  [(c), (d)],  $(0, 0.1)$  [(e), (f)], and  $(0.05, 0.1)$  [(g), (h)].  $N = 10$ .

In addition, we note that for a given Fermi level, the MoS<sub>2</sub> ZNRs behaves as a quantum valley Hall (QVH) phase [25,37]. This follows from the metallic edge modes in zigzag TMDC nanoribbons being valley locked, while the semiconductor edge modes of armchair TMDC nanoribbons are valley mixed and thus make the valley degree of freedom no longer a good quantum number [25,33]. Note that the QVH phase also implies possible emergence of valley-polarized edge current as a result of spin-valley locking.

In Figs. 5(c) and 5(d), we show the band structures including RSOC with  $\lambda_R = 0.05$  eV, for MoS<sub>2</sub> and WS<sub>2</sub> ZNRs, respectively. In contrast to the bulk 2D monolayer where the spin is degenerate in the  $\Gamma$  point, here we can see a spin state splitting even at  $k_x = 0$ , leading to minigaps. This feature may create a helical regime, i.e., the orientation of spin-up and spin-down branches might change when crossing this point. This peculiarity is essential to generate spin polariza-

tion of charge currents in quantum transport measurements. These minigaps are necessary for topological superconductivity states [38].

Now, we turn to the effect of exchange interaction. Figures 5(e) and 5(f) show the band structures of MoS<sub>2</sub> and WS<sub>2</sub> ZNRs nanoribbons only in the presence of exchange field with  $\lambda_{ex} = 0.1$  eV. We consider the exchange field oriented along the  $z$  direction, i.e., parallel to the spin quantization axis. Clearly, the spin-up and spin-down branches of the band structures are asymmetric with respect to  $k_x = 0$  because time-reversal symmetry is broken in the presence of exchange field. Note also that the spin remains a good quantum number, in contrast to the cases including only the RSOC, cf. Figs. 5(c) and 5(d) for MoS<sub>2</sub> and Figs. 5(e) and 5(f) for WS<sub>2</sub>.

In Figs. 5(g) and 5(h), we plot the combined effect of RSOC and exchange field interaction on the electronic band

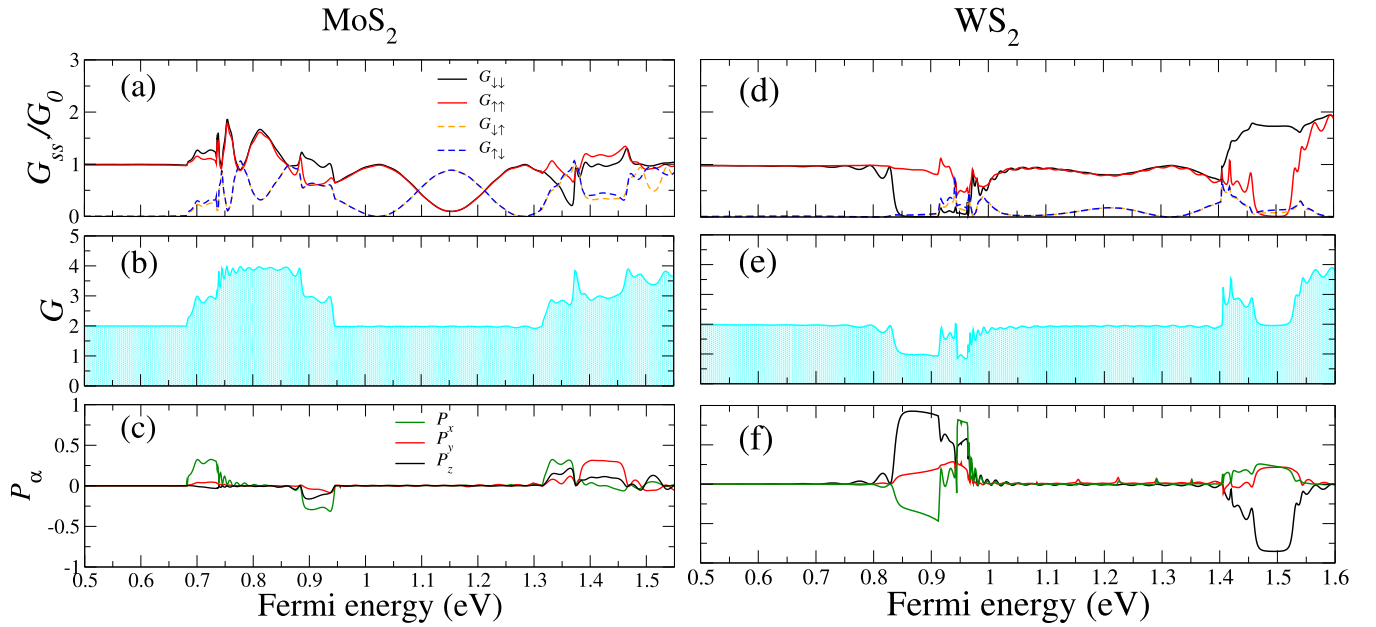


FIG. 6. (a), (d) Spin-resolved quantum conductances  $G_{ss'}$  in units of  $G_0$ , containing spin-conserved components ( $G_{\downarrow\downarrow}$ ,  $G_{\uparrow\uparrow}$ ) and spin-flip components ( $G_{\downarrow\uparrow}$ ,  $G_{\uparrow\downarrow}$ ); (b), (e) total quantum conductance  $G$ , and (c), (f) spin polarization  $P_\alpha$  along  $\alpha = x$  (blue color),  $y$  (red color), and  $z$  (black color) directions as a function of the Fermi energy in TMDC ZNRs with  $N = 10$  and  $l = 30$  with  $\lambda_R = 0.05$  eV. Results for MoS<sub>2</sub> (left panels) and WS<sub>2</sub> (right panels) ZNRs are shown, where  $N$  and  $l$  denote the numbers of zigzag lines along the transverse direction and the length of the central conductor in number of unit cells, respectively.

structure for MoS<sub>2</sub> and WS<sub>2</sub> ZNRs, respectively. As we can see, the contribution of the exchange interaction is mainly present at the band-edge states where the spins are almost well defined. In this case, the strength of the exchange field is bigger than the extrinsic RSOC and it would cause  $P_z$  to be larger than  $P_x$  and  $P_y$ , as we will see below.

### E. Effects of RSOC and exchange field on the spin quantum conductance and spin polarization of carrier current

In our calculations, we consider that the central region and two semi-infinite leads which are made of the same TMDC nanoribbon, as shown in Fig. 1. Accordingly, we include the intrinsic SOC throughout the whole system (both the central region and the two leads), while the RSOC and exchange field only appear in the central region. The Fermi energy is controlled by applying a gate voltage. As analyzed previously, the particle-hole symmetry in these structures is not preserved because the conduction and valence bands are mainly dominated by  $|d_{z^2}\rangle$  and  $|d_{x^2-y^2}\rangle \pm i|d_{xy}\rangle$  orbitals of the transition metal atom, respectively. Additionally, due to the asymmetry of the edges in TMDC ZNRs, composed of different atomic species, the transverse reflection symmetry in these systems is broken, in contrast to the case of ZGNRs [15]. Consequently, it is expected that perpendicular ( $P_z$ ) and parallel ( $P_x$ ) spin polarizations are not zero, in contradistinction to pristine ZGNRs [14–16]. For the quantum transport calculations, we consider the central region having width  $N$  and length  $l$  along the transverse ( $y$ ) and transport ( $x$ ) directions, respectively, with  $N = 10$  and  $l = 30$  denoting the number of unit cells [Fig. 1(b)], corresponding to 47.49 nm for MoS<sub>2</sub> and 47.29 nm for WS<sub>2</sub> ribbons.

In the left panel of Fig. 6, we show the spin-resolved quantum conductance  $G_{ss'}$  in units of  $G_0$  [Fig. 6(a)], total quantum conductance ( $G$ ) defined by Eq. (9) [Fig. 6(b)], and all three components ( $P_x$ ,  $P_y$ , and  $P_z$ ) of the spin polarization [Fig. 6(c)] for MoS<sub>2</sub> ZNRs at  $\lambda_R = 0.05$  eV. The corresponding results for WS<sub>2</sub> ZNRs are shown in Figs. 6(d)–6(f), respectively, namely, in the right panels of Figs. 6. Below we describe the quantum transport properties by comparing the characteristics of MoS<sub>2</sub> and WS<sub>2</sub> ZNRs. In Figs. 6(a) and 6(d), the conductance components do not exhibit perfect plateaus; oscillations are observed in both MoS<sub>2</sub> and WS<sub>2</sub> ZNRs, as also happens in ZGNRs [29,39]. It is known that the amplitude of these oscillations depends on the length of the central part  $l$  and it decreases as  $l$  increases, analogous to the spin field effect transistor, in which the spin rotates as it moves across the conductor due to the Rashba field [29,40,41]. Furthermore, the spin-conserved and spin-flip conductances are different for all spin projection directions, i.e.,  $G_{\uparrow\uparrow} \neq G_{\downarrow\downarrow}$  and  $G_{\downarrow\uparrow} \neq G_{\uparrow\downarrow}$ , due to the longitudinal asymmetry in these structures. This is in contrast to ZGNRs, where  $G_{\uparrow\uparrow} = G_{\downarrow\downarrow}$  and  $G_{\downarrow\uparrow} = G_{\uparrow\downarrow}$  if the width of the ribbons ( $N$ ) is even and intrinsic SOC is zero but RSOC is present. More specifically, in MoS<sub>2</sub> ZNRs [Fig. 6(a)], the conductance from spin-flip contribution is comparable to the spin-conserved one, being in almost opposite phases. In other words, when the spin-flip contribution is vanishing, the spin-conserving one attains its maximum, and vice versa. However, in WS<sub>2</sub> ZNRs [Fig. 6(d)], we find that the spin-conserved conductance dominates over the spin-flip term. This feature is attributed to the interplay between intrinsic SOC and RSOC: The former favors the spin polarization along the vertical direction, while the latter tends to rotate the spin. Since the intrinsic SOC in WS<sub>2</sub> is much

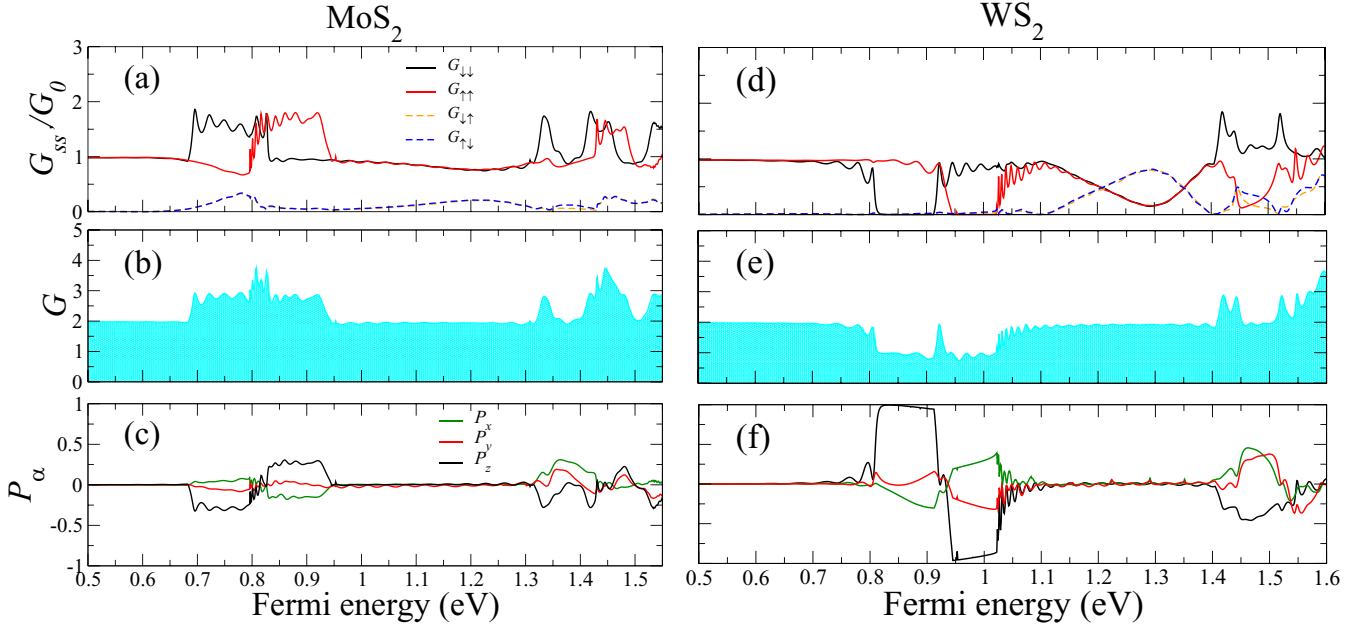


FIG. 7. (a), (d) Spin-resolved quantum conductances  $G_{ss}$  in units of  $G_0$ , containing spin conserving components ( $G_{\downarrow\downarrow}$ ,  $G_{\uparrow\uparrow}$ ) and spin-flip components ( $G_{\downarrow\uparrow}$ ,  $G_{\uparrow\downarrow}$ ); (b), (e) total quantum conductance  $G$ , and (c), (f) spin polarization  $P_\alpha$  along  $\alpha = x$  (blue color),  $y$  (red color), and  $z$  (black color) directions as a function of the Fermi energy in TMDC ZNRs with  $N = 10$  and  $l = 30$  with  $\lambda_R = 0.05$  eV and  $\lambda_{ex} = 0.1$  eV. Results for MoS<sub>2</sub> (left panels) and WS<sub>2</sub> (right panels) ZNRs are shown, where  $N$  and  $l$  denote the numbers of zigzag lines along the transverse direction and the length of the central conductor in number of unit cells, respectively.

stronger, the spin-conserved conductance is larger than the spin-flip one.

Figures 6(b) and 6(e) show the total quantum conductance of MoS<sub>2</sub> and WS<sub>2</sub> ZNRs, respectively. For MoS<sub>2</sub> ZNRs, there are intervals of energy ranging from 0 to 0.7 eV and from 0.95–1.3 eV, in which the total conductance shows almost perfect plateaus. In addition, the minimum total value is  $2G_0$ , see Fig. 6(b). In contrast, for WS<sub>2</sub> ZNRs, the minimum total conductance is less than  $2G_0$ , cf. Figs. 6(b) and 6(e). It is worth noting that these conductance plateaus are directly associated with the peaks of DOS shown in Fig. 4.

With respect to the spin polarizations, shown in Fig. 6(c), we find that the largest contribution to the polarization in MoS<sub>2</sub> comes from  $P_x$  and  $P_y$  components. Between them, the  $P_x$  component can reach more than 25% in magnitude, both with positive and negative signs. Along the transverse direction, the corresponding spin polarization ( $P_y$ ) has similar values to  $P_x$  while only positive values are observed in an interval of 1.39–1.46 eV for the Fermi energy. In addition, this feature is strongly dependent on the intrinsic SOC and is in contrast to pristine ZGNRs, where only the transverse component is non-negligible [15]. Specifically, unusual  $P_x$  and  $P_z$  components in WS<sub>2</sub> ZNRs are observed [Fig. 6(f)], and we find that the  $P_z$  component dominates over the other polarizations, reaching 90% both with positive and negative signs. This is due to the minigap at  $k_x = 0$  in the band structure. These remarkable quantitative results show that our system can behave as a spin filter. Additionally, we observe that the longitudinal component can reach considerable values when we vary the intensity of the RSOC.

Let us turn now to the more realistic case in which both the exchange field interaction and RSOC are taken into account in

the quantum conductance and spin polarization. In Fig. 7, we show the spin-resolved quantum conductances, total quantum conductance, and spin polarization for MoS<sub>2</sub> (left panel) and WS<sub>2</sub> (right panel) ZNRs. Here we choose  $\lambda_{ex} = 0.1$  eV and keep the same value of RSOC parameter  $\lambda_R = 0.05$  eV used above. From Figs. 7(a) and 7(d), we find that the interplay of the two interactions reverses the dominant contributions to the conductance between the spin-conserved and spin-flip ones, as compared to the case that only RSOC is present, cf. Figs. 6(a) and 7(a) for MoS<sub>2</sub> ZNRs and cf. Figs. 6(d) and 7(d) for WS<sub>2</sub> ZNRs. This is because the exchange term directly affects the spin-conserved components of the conductance. It is also manifested in the spin polarization plotted in Figs. 7(e) and 7(f), for MoS<sub>2</sub> and WS<sub>2</sub> ZNRs, respectively. It is found that the  $P_z$  component in MoS<sub>2</sub> ZNRs reaches almost 30% both with positive and negative signs, while the  $P_x$  and  $P_y$  components decrease considerably when  $\lambda_{ex}$  is absent, see, for instance, Fig. 6(c). Most interestingly, for WS<sub>2</sub> ZNRs, the  $P_z$  component of the spin polarization can reach almost 100% in both positive and negative values. On the other hand, the values of  $P_x$  and  $P_y$  decrease considerably. This indicates that the effect of exchange field interaction is more important in W-based TMDC ribbons than in Mo-based ones.

To gain deeper insight on spin polarization, we further explore the dependence of spin polarization on the RSOC parameter and the Fermi energy. In Figs. 8(a)–8(d), we show the contour of three components ( $P_x$ ,  $P_y$ , and  $P_z$ ) of spin polarization, and the total polarization ( $P_T$ ) as functions of RSOC and Fermi energy for MoS<sub>2</sub> ZNRs. We have omitted the exchange field in the calculation to elucidate the effect of RSOC. Let us start with the  $P_x$  component [Fig. 8(a)]. We observe three branches of spin polarization at different Fermi

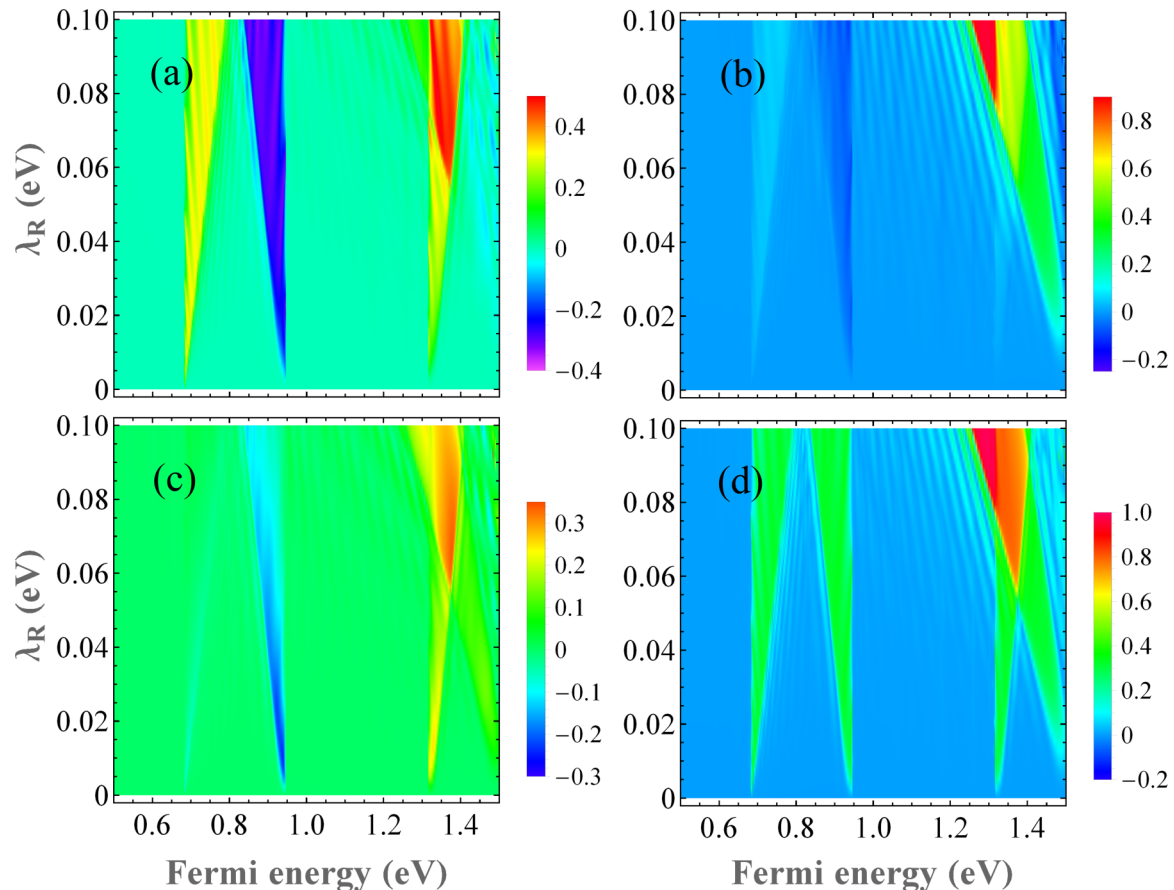


FIG. 8. Contour of the three components,  $P_x$  (a),  $P_y$  (b),  $P_z$  (c), and the total  $P_t$  (d) of spin polarization for a MoS<sub>2</sub> ZNR with  $N = 10$  and  $l = 30$  as a function of RSOC parameter and Fermi energy.

energies, which correspond to the three minigaps in the band structure, see Fig. 5(c). Interestingly, the  $P_x$  is positive (yellow color) in the energy range of 0.7–0.8 eV, while it becomes negative (blue color) when the Fermi energy lies in the range of 0.85–1.0 eV. It becomes positive again (red and yellow colors for higher and lower RSOC parameters, respectively) as the Fermi energy further increases (1.3–1.4 eV). On the other hand, for each of the three branches, the energy range quenches considerably as the RSOC parameter decreases. This is because the minigaps decrease in the band structure with diminishing RSOC parameter.

The dependence of  $P_y$  and  $P_z$  components on the RSOC strength and Fermi energy are displayed in Figs. 8(b) and 8(c). We also find three branches in the same energy range as  $P_x$ . Nevertheless, the magnitude of  $P_y$  and  $P_z$  is smaller than that of  $P_x$ . Interestingly, at specific values of the Fermi energy and high RSOC,  $P_t$  can reach its maximum value 100% (red color), see Fig. 8(d).

In Fig. 9, we show the spin-polarization components and its total value for WS<sub>2</sub> ZNRs in contour plots. Similar to MoS<sub>2</sub> ZNRs, there are three branches at different Fermi energies for each component. Among them, the first two branches almost collapse at the same energy, because two of the three minigaps in the band structure almost coincide [Fig. 5(d)]. Our results show that  $P_x$  rises above 50% with negative sign for larger

RSOC strengths, and more than 75% in positive value but in a different energy range. In addition, the  $P_z$  component is much stronger than  $P_x$  and  $P_y$  WS<sub>2</sub> ZNRs, in contrast to MoS<sub>2</sub> ZNRs, for which the  $P_x$  component is the strongest. This follows from the fact that spin mixing around  $k_x = 0$  is much weaker in W-based TMDCs than in Mo-based ones, due to the larger intrinsic SOC of W.

As for the total polarization  $P_t$  [Fig. 9(d)], it can attain 100% in all three branches within a large energy range, as opposed to in MoS<sub>2</sub> ZNRs, where  $P_t \sim 100\%$  only occurs in one branch. We demonstrate that devices made of TMDC ZNRs possess polarization in different directions even in the absence of defects and/or impurities that were essential for ZGNRs. [27] This is in stark contrast to the case of graphene, in which only the spin polarization along the transverse direction ( $P_y$ ) survives under the condition that the transverse reflection symmetry maintains [15]. We find that intrinsic SOC is a key ingredient for the emergence of nonzero polarization in all directions. From an experimental point of view, we note that it is feasible to measure all three components of the spin polarization by using a Wien filter and Mott detector [27,42].

Bear in mind that the valley-polarized edge current in TMDC zigzag ribbons can be inferred because spin and valley are locked together. It is worthy to comment that the presence of a high concentration of disorders or edge

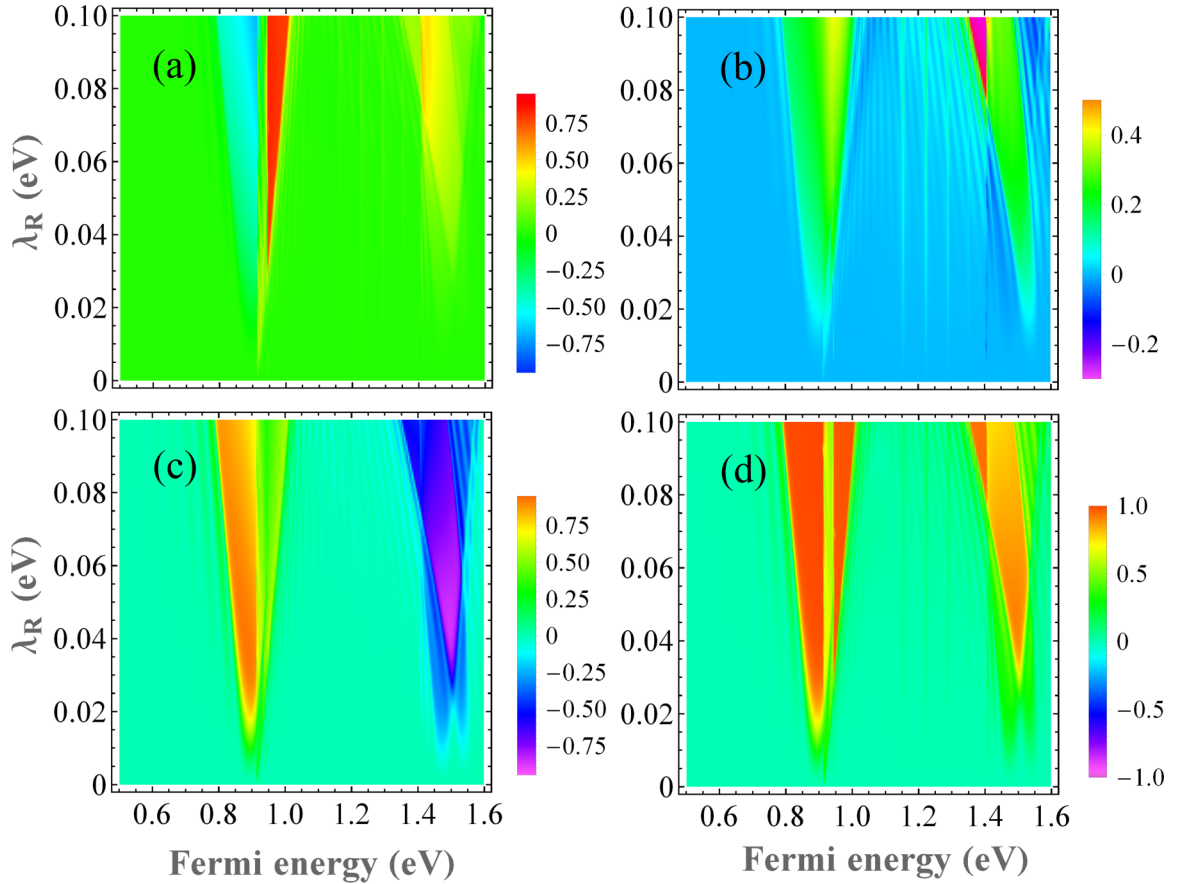


FIG. 9. Contour of the three components,  $P_x$  (a),  $P_y$  (b),  $P_z$  (c), and the total  $P_t$  (d) of spin polarization for a  $\text{WS}_2$  ZNR with  $N = 10$  and  $l = 30$  as a function of RSOC parameter and Fermi energy.

vacancies might affect the transport properties of TMDC ZNRs [33].

#### IV. CONCLUSIONS

In summary, we report anisotropic spin-polarized edge currents through  $\text{MoS}_2$  and  $\text{WS}_2$  monolayer ZNRs deposited on either nonmagnetic substrate or on FM insulators. We employ an 11-band TB model to calculate the electronic band structures of TMDC monolayers and their nanoribbons in the presence of RSOC and exchange field interaction. We adopt the nonequilibrium Green's function method together with Landauer-Büttiker formalism to study quantum transport through edge states. RSOC leads to a band crossing at  $\Gamma$  point that can be opened by an exchange field induced by magnetic proximity effect. We demonstrate that spin-polarized edge current can be generated in both  $\text{MoS}_2$  and  $\text{WS}_2$  ZNRs with RSOC. Unlike ZGNRs, in which spin polarization mainly occurs in the transverse direction, in TMDC nanoribbons it spreads out into all three directions. Interestingly, the largest spin-polarization component is not along the transversal direction of TMDC ZNRs. It depends strongly upon the intrinsic SOC, which is an essential ingredient for this effect. In the TMDCs with large intrinsic SOC such as  $\text{WS}_2$  monolayer ZNR, the largest polarization is along the  $z$  direction. In addition, the magnetic proximity effect favors this anisotropy. For  $\lambda_{\text{ex}} = 0.1$  eV, high efficient spin filtering behaviors are found in both materials. For instance,  $P_z$  can reach more than

90% in  $\text{WS}_2$  NRs. The anisotropy of the spin polarization can be experimentally measured by Mott polarimeters [42,43]. We expect that our results should stimulate relevant experimental investigations for these 1D systems.

#### ACKNOWLEDGMENTS

This work was supported by CNPq, CAPES, FAPDF, the Research Fund of Qufu Normal University, and the National Natural Science Foundation of China (Grants No. 11004120 and No. 11874236). L.C. acknowledges financial support of the Spanish MINECO and the European Union under Grants No. FIS2015-64654 P/MINECO/FEDER and No. PGC2018-097018-B-I00. J.H.C. thanks Dr. Sudy Ganguly for helpful discussions.

#### APPENDIX A: RASHBA FIELD IN TMDC ZIGZAG NANORIBBON

The basis set we consider for TMDC ZNR is given by  $|d_z\rangle, |d_{xy}\rangle, |d_{x^2-y^2}\rangle, |p_z^e\rangle, |p_x^e\rangle, |p_y^e\rangle \otimes |\uparrow, \downarrow\rangle$ , where  $p_z^e = \frac{1}{\sqrt{2}}(p_z^t - p_z^b)$ ,  $p_x^e = \frac{1}{\sqrt{2}}(p_x^t + p_x^b)$  and  $p_y^e = \frac{1}{\sqrt{2}}(p_y^t + p_y^b)$  [25]. The matrix elements for the Rashba term can be

written as

$$H_R^B(\vec{r}) = \begin{pmatrix} 0 & 0 & 0 & 0 & 0 & 0 & h_R & 0 & 0 & 0 & 0 & 0 \\ 0 & 0 & 0 & 0 & 0 & 0 & 0 & h_R & 0 & 0 & 0 & 0 \\ 0 & 0 & 0 & 0 & 0 & 0 & 0 & 0 & h_R & 0 & 0 & 0 \\ 0 & 0 & 0 & 0 & 0 & 0 & 0 & 0 & 0 & h_R & 0 & 0 \\ 0 & 0 & 0 & 0 & 0 & 0 & 0 & 0 & 0 & 0 & h_R & 0 \\ 0 & 0 & 0 & 0 & 0 & 0 & 0 & 0 & 0 & 0 & 0 & h_R \\ h_R^* & 0 & 0 & 0 & 0 & 0 & 0 & 0 & 0 & 0 & 0 & 0 \\ 0 & h_R^* & 0 & 0 & 0 & 0 & 0 & 0 & 0 & 0 & 0 & 0 \\ 0 & 0 & h_R^* & 0 & 0 & 0 & 0 & 0 & 0 & 0 & 0 & 0 \\ 0 & 0 & 0 & h_R^* & 0 & 0 & 0 & 0 & 0 & 0 & 0 & 0 \\ 0 & 0 & 0 & 0 & h_R^* & 0 & 0 & 0 & 0 & 0 & 0 & 0 \\ 0 & 0 & 0 & 0 & 0 & h_R^* & 0 & 0 & 0 & 0 & 0 & 0 \\ 0 & 0 & 0 & 0 & 0 & 0 & h_R^* & 0 & 0 & 0 & 0 & 0 \end{pmatrix},$$

with  $h_R = i\frac{\lambda_R}{a}(\vec{r} \cdot \hat{y} + i\vec{r} \cdot \hat{x})$  and

$$\begin{aligned} H_R &= H_{B4}|m, n\rangle\langle m, n+4| + H_{B5}|m, n\rangle\langle m, n-4| \\ &\times H_{B2}(|m, n\rangle\langle m+1, n+2| + |m, n\rangle\langle m-1, n+2|) \\ &\times H_{B3}(|m, n\rangle\langle m+1, n-2| + |m, n\rangle\langle m-1, n-2|), \end{aligned} \quad (\text{A1})$$

where

$$H_{B2} = H_R^B(\vec{C}_1) + H_R^B(\vec{C}_3), \quad (\text{A2})$$

$$H_{B3} = H_R^B(\vec{C}_4) + H_R^B(\vec{C}_6), \quad (\text{A3})$$

$$H_{B4} = H_R^B(\vec{C}_2), \quad (\text{A4})$$

$$H_{B5} = H_R^B(\vec{C}_5). \quad (\text{A5})$$

Here  $B = M, X$  denotes the transition metal and chalcogen atoms, respectively.  $H_R$  is the corresponding Rashba Hamiltonian. The kets and bras are defined with respect to the coordinates relative to the site  $(m, n)$  and  $\vec{C}_1, \vec{C}_2, \dots, \vec{C}_6$  are hopping vectors connecting different sites and the values are given in Ref. [25].

## APPENDIX B: EXCHANGE INTERACTION IN TMDC ZIGZAG NANORIBBON

The matrix Hamiltonian of the exchange field produced by a FM substrate perpendicular to the monolayer plane is given by

$$h_{\text{ex}} = \begin{pmatrix} \lambda_{\text{ex}} & 0 & 0 & 0 & 0 & 0 \\ 0 & \lambda_{\text{ex}} & 0 & 0 & 0 & 0 \\ 0 & 0 & \lambda_{\text{ex}} & 0 & 0 & 0 \\ 0 & 0 & 0 & \lambda_{\text{ex}} & 0 & 0 \\ 0 & 0 & 0 & 0 & \lambda_{\text{ex}} & 0 \\ 0 & 0 & 0 & 0 & 0 & \lambda_{\text{ex}} \end{pmatrix} \otimes \begin{pmatrix} 1 & 0 \\ 0 & -1 \end{pmatrix}, \quad (\text{B1})$$

and

$$H_{\text{ex}} = h_{\text{ex}}|m, n\rangle\langle m, n|. \quad (\text{B2})$$

## APPENDIX C: THE RECURSIVE GREEN'S FUNCTION METHOD

The Green's function can be written as

$$(E \pm i\epsilon - H)\mathcal{G} = I. \quad (\text{C1})$$

By projecting into the right layer orbitals and using the Dyson's equation, we get a set of equations [31],

$$\begin{aligned} (E \pm i\epsilon - H_{00})\mathcal{G}_{00} &= I + H_{01}^\dagger \mathcal{G}_{10}, \\ (E \pm i\epsilon - H_{00})\mathcal{G}_{10} &= H_{01}^\dagger \mathcal{G}_{00} + H_{01} \mathcal{G}_{20}, \\ (E \pm i\epsilon - H_{00})\mathcal{G}_{20} &= H_{01} \mathcal{G}_{10} + H_{01} \mathcal{G}_{30}, \\ &\vdots \\ (E \pm i\epsilon - H_{00})\mathcal{G}_{n0} &= H_{01}^\dagger \mathcal{G}_{n-1,0} + H_{01} \mathcal{G}_{n+1,0}, \end{aligned} \quad (\text{C2})$$

where  $E$  is the energy of the incoming electron,  $H_{nm}$  are the matrix elements of the TB Hamiltonian, and  $\mathcal{G}_{nm}$  is the Green's function. We consider the leads are pristine (i.e., without any disorder), which ensures the relation  $H_{00} = H_{11} = \dots = H_{nn}$  and  $H_{01} = H_{12} = \dots = H_{n-1n}$  with the latter denoting the the matrix elements connecting different layers. With the help of the transfer matrices  $T$  and  $\bar{T}$ , we can obtain a chain of layers to connect the Green's function of an individual layer using the previous and next layer, such that  $\mathcal{G}_{00} = \bar{T}\mathcal{G}_{10}$  and  $\mathcal{G}_{10} = T\mathcal{G}_{00}$ . The transfer matrix elements are given by [30,31]

$$T = t_0 + \tilde{t}_0 t_1 + \tilde{t}_0 \tilde{t}_1 t_2 + \dots + \tilde{t}_0 \tilde{t}_1 \tilde{t}_2 \dots t_n, \quad (\text{C3})$$

$$\bar{T} = \tilde{t}_0 + t_0 \tilde{t}_1 + t_0 t_1 \tilde{t}_2 + \dots + t_0 t_1 t_2 \dots \tilde{t}_n, \quad (\text{C4})$$

where  $t_i$  and  $\tilde{t}_i$  describe the recursion relation:

$$t_i = (I - t_{i-1} \tilde{t}_{i-1} - \tilde{t}_{i-1} t_{i-1})^{-1} t_{i-1}^2, \quad (\text{C5})$$

$$\tilde{t}_i = (I - t_{i-1} \tilde{t}_{i-1} - \tilde{t}_{i-1} t_{i-1})^{-1} \tilde{t}_{i-1}^2. \quad (\text{C6})$$

To obtain  $T$  and  $\bar{T}$ , an iteration procedure is adopted. We start with the iteration from the principal

layer, i.e.,

$$t_0 = (E \pm i\epsilon - H_{00})^{-1} H_{01}^\dagger, \quad (\text{C7})$$

$$\bar{t}_0 = (E \pm i\epsilon - H_{00})^{-1} H_{01}. \quad (\text{C8})$$

Then, we repeat the process until the convergence is attained, i.e.,  $t_n, \bar{t}_n \leq \delta$ , with  $\delta$  a small quantity defining the precision of the convergence.

- 
- [1] A. H. Castro Neto, F. Guinea, N. M. R. Peres, K. S. Novoselov, and A. K. Geim, *Rev. Mod. Phys.* **81**, 109 (2009).
- [2] D. Xiao, G.-B. Liu, W. Feng, X. Xu, and W. Yao, *Phys. Rev. Lett.* **108**, 196802 (2012).
- [3] F. Wu, F. Qu, and A. H. MacDonald, *Phys. Rev. B* **91**, 075310 (2015).
- [4] A. Kormányos, G. Burkard, M. Gmitra, J. Fabian, V. Zólyomi, N. D. Drummond, and V. Falko, *2D Materials* **2**, 022001 (2015).
- [5] G.-B. Liu, W.-Y. Shan, Y. Yao, W. Yao, and D. Xiao, *Phys. Rev. B* **88**, 085433 (2013).
- [6] K. Kośmider, J. W. González, and J. Fernández-Rossier, *Phys. Rev. B* **88**, 245436 (2013).
- [7] H. Bragança, F. Riche, F. Qu, V. Lopez-Richard, and G. E. Marques, *Sci. Rep.* **9**, 4575 (2019).
- [8] H. Li, J. Shao, D. Yao, and G. Yang, *ACS Appl. Mater. Interfaces* **6**, 1759 (2014).
- [9] I. Žutić, J. Fabian, and S. Das Sarma, *Rev. Mod. Phys.* **76**, 323 (2004).
- [10] J. R. Schaibley, H. Yu, G. Clark, P. Rivera, J. S. Ross, K. L. Seyler, W. Yao, and X. Xu, *Nat. Rev. Mater.* **1**, 16055 (2016).
- [11] Y. Chen, P. Cui, X. Ren, C. Zhang, C. Jin, Z. Zhang, and C.-K. Shih, *Nat. Commun.* **8**, 15135 (2017).
- [12] F. Cheng, H. Xu, W. Xu, P. Zhou, J. Martin, and K. P. Loh, *Nano Lett.* **17**, 1116 (2017).
- [13] Z. Wang, X. Zhang, J. A. Hachtel, A. Apte, C. S. Tiwary, R. Vajtai, J. C. Idrobo, R. Ozturk, and P. Ajayan, *Nanoscale Horiz.* **4**, 689 (2019).
- [14] L. Chico, A. Latgé, and L. Brey, *Phys. Chem. Chem. Phys.* **17**, 16469 (2015).
- [15] J.-F. Liu, K. S. Chan, and J. Wang, *Nanotechnology* **23**, 095201 (2012).
- [16] Q. Zhang, K. S. Chan, and J. Li, *Phys. Chem. Chem. Phys.* **19**, 6871 (2017).
- [17] Q. Zhang, J. Jiang, and K. S. Chan, *Phys. Lett. A* **383**, 2957 (2019).
- [18] H. Santos, A. Latgé, L. Brey, and L. Chico, *arXiv:1908.07629* [cond-mat.mes-hall].
- [19] J. Qi, X. Li, Q. Niu, and J. Feng, *Phys. Rev. B* **92**, 121403(R) (2015).
- [20] Q. Zhang, S. A. Yang, W. Mi, Y. Cheng, and U. Schwingenschlögl, *Adv. Mater.* **28**, 959 (2016).
- [21] C. Zhao, T. Norden, P. Zhang, P. Zhao, Y. Cheng, F. Sun, J. P. Parry, P. Taheri, J. Wang, Y. Yang, T. Scrace, K. Kang, S. Yang, G.-x. Miao, R. Sabirianov, G. Kioseoglou, W. Huang, A. Petrou, and H. Zeng, *Nat. Nanotechnol.* **12**, 757 (2017).
- [22] T. Norden, C. Zhao, P. Zhang, R. Sabirianov, A. Petrou, and H. Zeng, *Nat. Commun.* **10**, 4163 (2019).
- [23] D. Zhong, K. L. Seyler, X. Linpeng, R. Cheng, N. Sivadas, B. Huang, E. Schmidgall, T. Taniguchi, K. Watanabe, M. A. McGuire, W. Yao, D. Xiao, K.-M. C. Fu, and X. Xu, *Sci. Adv.* **3**, e1603113 (2017).
- [24] Z. Wang, C. Tang, R. Sachs, Y. Barlas, and J. Shi, *Phys. Rev. Lett.* **114**, 016603 (2015).
- [25] A. C. Dias, F. Qu, D. L. Azevedo, and J. Fu, *Phys. Rev. B* **98**, 075202 (2018).
- [26] K. Lee, W. S. Yun, and J. D. Lee, *Phys. Rev. B* **91**, 125420 (2015).
- [27] S. Ganguly, S. Basu, and S. K. Maiti, *Europhys. Lett.* **124**, 57003 (2018).
- [28] J. H. Correa, A. Pezo, and M. S. Figueira, *Phys. Rev. B* **98**, 045419 (2018).
- [29] G. S. Diniz, M. R. Guassi, and F. Qu, *J. Appl. Phys.* **116**, 113705 (2014).
- [30] M. Buongiorno Nardelli, *Phys. Rev. B* **60**, 7828 (1999).
- [31] M. P. L. Sancho, J. M. L. Sancho, and J. Rubio, *J. Phys. F: Metal Phys.* **14**, 1205 (1984).
- [32] P.-H. Chang, F. Mahfouzi, N. Nagaosa, and B. K. Nikolić, *Phys. Rev. B* **89**, 195418 (2014).
- [33] E. Ridolfi, L. R. F. Lima, E. R. Mucciolo, and C. H. Lewenkopf, *Phys. Rev. B* **95**, 035430 (2017).
- [34] B. Scharf, G. Xu, A. Matos-Abiague, and I. Žutić, *Phys. Rev. Lett.* **119**, 127403 (2017).
- [35] N. M. R. Peres, A. H. Castro Neto, and F. Guinea, *Phys. Rev. B* **73**, 195411 (2006).
- [36] R.-L. Chu, G.-B. Liu, W. Yao, X. Xu, D. Xiao, and C. Zhang, *Phys. Rev. B* **89**, 155317 (2014).
- [37] B. T. Zhou, K. Taguchi, Y. Kawaguchi, Y. Tanaka, and K. T. Law, *Comm. Phys.* **2**, 26 (2019).
- [38] G. Xu, J. Wang, B. Yan, and X.-L. Qi, *Phys. Rev. B* **90**, 100505(R) (2014).
- [39] M. Karimnizhad and A. Namiranian, *J. Appl. Phys.* **110**, 103702 (2011).
- [40] S. Datta and B. Das, *Appl. Phys. Lett.* **56**, 665 (1990).
- [41] B. Radisavljevic, A. Radenovic, J. Brivio, V. Giacometti, and A. Kis, *Nat. Nanotechnol.* **6**, 147 (2011).
- [42] E. Kisker, *Rev. Sci. Instrum.* **53**, 507 (1982).
- [43] F. Meier, J. H. Dil, and J. Osterwalder, *New J. Phys.* **11**, 125008 (2009).